DOI: 10.1002/chem.200801236

Heterometal Alkoxides as Precursors for the Preparation of Porous Fe– and Mn–TiO_2 Photocatalysts with High Efficiencies

Xiao-Xin Zou,[a] Guo-Dong Li,[a] Ming-Yi Guo,[a] Xin-Hao Li,[a] Da-Peng Liu,[a] Juan Su,[a] and Jie-Sheng Chen*[a, b]

Abstract: Transition-metal-doped titanium glycolates (M–TG, with M = Fe, Mn), which are the first non-stoichiometric heterometal alkoxides, have been synthesised through a solvothermal doping approach. X-ray diffraction, UV/Vis diffuse reflectance and ESR spectroscopy revealed that the dopant ion (Fe^{3+} or Mn^{2+}) is substituted for Ti^{4+} in the TG lattice. Fe^{3+} prolongs the crystallisation time of Fe–TG, whereas Mn^{2+} has a smaller effect on the crystallisation time in comparison with Fe^{3+}. The as-synthesised M–TG materials were used directly as single-source precursors for the preparation of metal-doped titania (M–TiO_2) through a simple thermal treatment process. The as-prepared M–TiO_2 materials maintain the rod-like morphology of the precursors and possess a mesoporous structure with high crystallinity. It has been proved that the dopant ions are incorporated into the TiO_2 lattice at the Ti^{4+} positions. The photocatalytic activities of the M–TiO_2 materials obtained were evaluated by testing the degradation of phenol under UV irradiation. From the photocatalytic results, it was concluded that high crystallinity, a large surface area and appropriate transition-metal-doping are all beneficial to the enhancement of the photocatalytic performance of the doped TiO_2 material. In addition, it was noted that in comparison with Mn–TiO_2, Fe–TiO_2 shows higher photocatalytic activity due to the better inhibition effect of Fe^{3+} on recombination of photogenerated electron–hole pairs. In contrast to the conventional nanosized TiO_2 photocatalyst, the micrometre-sized M–TiO_2 particles we obtained can be easily separated and recovered after the photocatalytic reactions.

Keywords: glycolates • photocatalysis • porous materials • titanium • transition metals

Introduction

Nanosized TiO_2, which exhibits photocatalytic activity superior to that of bulk TiO_2 due to its large surface area, is expected to play an important role in helping solve many environmental problems.[1,2] However, the practical application of nanosized TiO_2 materials in the elimination of pollutants from water suffers from difficulties in the separation and recovery of the photocatalysts. Immobilisation of nanosized TiO_2 particles on a support can successfully solve the problem of separation, but the efficiency of photocatalysis under this circumstance decreases drastically owing to a significant loss of the photocatalytically active area.[3,4]

Recently, submicrometre- and micrometre-sized TiO_2 photocatalysts with a porous structure have garnered increasing interest because these photocatalytic materials are easier to separate from solution, but they also possess significant surface areas, and hence, their photocatalytic performances are comparable to those of the corresponding nanoparticle materials.[5–8] Although much effort has been devoted to the synthesis of porous TiO_2 photocatalysts, there are still many barriers to the targeted products. The first difficulty results from the uncontrollable sol–gel process that results from a high hydrolysis–condensation rate of titanium precursors.[9] The second difficulty is the thermal instability of the inorganic network during crystallisation of titanium oxide. Calcination of the as-prepared porous titania material often leads to a dense and fully collapsed structure because of the intrinsic crystallisation of the anatase phase.[9–12] To

---

[a] X.-X. Zou, Prof. G.-D. Li, M.-Y. Guo, X.-H. Li, D.-P. Liu, J. Su, Prof. J.-S. Chen
State Key Laboratory of Inorganic Synthesis and
Preparative Chemistry
College of Chemistry, Jilin University
Changchun 130012 (P.R. China)
E-mail: chemcj@sjtu.edu.cn

[b] Prof. J.-S. Chen
School of Chemistry and Chemical Engineering
Shanghai Jiao Tong University, Shanghai 200240 (P.R. China)
Fax: (+86) 21-5474-1297

Supporting information for this article is available on the WWW under http://dx.doi.org/10.1002/chem.200801236.

solve these problems, a sophisticated synthetic scheme is usually necessary and the synthetic conditions are rather restrictive. Therefore, facile approaches to the preparation of submicrometre- and micrometre-sized TiO_2 photocatalysts with a porous structure are highly desired. In addition, it is known that the doping of transition metals such as iron and manganese into TiO_2 may suppress the recombination rates of photogenerated electrons and holes, and hence, improve the photocatalytic performance of TiO_2-based catalysts.[1,13–20] Therefore, it is expected that the combination of porosity with metal-doping in TiO_2 materials would achieve highly effective photocatalysts that are easy to separate from the corresponding reaction systems.

Metal alkoxides have been extensively investigated because they are important precursors for the preparation of inorganic–organic hybrid and oxide–ceramic materials.[21–24] Of the metal alkoxide compounds, titanium alkoxides, especially those containing heterometal atoms, have attracted enormous attention due to their wide application in various areas.[22,24–27] Nevertheless, the preparation of heterometal-containing titanium alkoxides reported to date is limited to stoichiometric compounds. In this paper, a doping strategy that realises the formation of non-stoichiometric titanium-based heterometal alkoxides is described for the first time. Furthermore, by using these heterometal alkoxides as precursors, crystalline porous M–TiO_2 (M = Fe, Mn) photocatalysts have been obtained through a simple thermal treatment process. In contrast to the conventional nanosized TiO_2 photocatalyst, the porous TiO_2 materials prepared through our approach can be easily separated and recovered after the photocatalytic reactions and still exhibit high photocatalytic activities.

Results and Discussion

Synthesis of heterometal alkoxides: For the preparation of the iron- and manganese-containing heterometal alkoxides, titanium glycolate (TG, $Ti(OCH_2CH_2O)_2$; monoclinic space group *C*2/*c* (no. 15), unit cell parameters $a = 15.204$, $b = 7.568$, $c = 5.816$ Å, $\beta = 110.87°$) was chosen as the host compound for the following reasons:[28] Firstly, unlike many titanium alkoxides with extreme moisture sensitivity, this compound is rather stable towards moisture. Secondly, in contrast to most crystalline titanium alkoxides with a zero-dimensional structure, TG is a crystalline complex with infinite one-dimensional chains (Figure 1) and this structural feature may benefit the conversion of the alkoxide into the titania material. Finally, the synthetic condition of the compound can be modified to allow for doping of heterometal atoms into the structure.

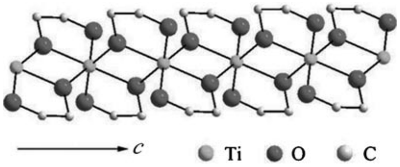

Figure 1. View of the one-dimensional chain of $Ti(OCH_2CH_2O)_2$ along the *c* axis.

Originally the reaction system for the preparation of TG was basic. Evidently such a system cannot fulfil our purpose of doping Fe^{3+} into TG because Fe^{3+} is sensitive to alkalinity and Fe_3O_4 easily forms from an alkaline system.[29,30] In addition, the reaction time reported previously for the formation of TG was rather long (5 d in total). In this context, we modified the synthetic procedure to a certain extent. Typically, $Ti(n\text{-}OBu)_4$ as the titanium source and $FeCl_3{\cdot}6H_2O$ as the iron source were added to ethylene glycol and the mixture was heated at 180 °C for 2–5 h. The content of Fe^{3+} added to the reaction system is represented by the molar ratio ($R_{Fe/(Ti+Fe)}$) of Fe to (Ti + Fe) in the reaction mixture. No base was added to the reaction system and highly crystalline Fe–TG was obtained by separation of the solid product from the reaction system. The yield of the product was nearly 100 % on the basis of the metal sources used. Furthermore, Mn^{2+} (content expressed as $R_{Mn/(Ti+Mn)}$) was also doped into TG to form Mn–TG through a synthetic procedure similar to that used for Fe–TG. Apart from Fe^{3+} and Mn^{2+}, a series of other 3d transition metals, including Cr^{3+}, Co^{2+}, Ni^{2+} and Cu^{2+}, were also used as dopants for the formation of M–TG compounds. However, these metal ions failed to be incorporated into the structure of the TG compound.

The structures of the as-synthesised Fe–TG and Mn–TG were confirmed by powder X-ray diffraction (XRD). The XRD patterns (Figure 2a and b) are coincident with that simulated on the basis of the single-crystal structure of TG (Figure S1 of the Supplementary Information). No diffraction peaks from impurity phases were observed even for the product with a Fe^{3+}-doping content as high as 9 %. Nevertheless, the incorporation of Fe^{3+} or Mn^{2+} into the TG crystal structure caused a shift of the diffraction peaks to lower angles. The interplanar spacing $d_{(200)}$ value (Figure 2c) calculated by the Bragg equation increases with the ratio $R_{Fe/(Ti+Fe)}$. This is rationalised by the fact that the Fe^{3+} ($r = 0.79$ Å) or Mn^{2+} ion ($r = 0.80$ Å) is distinctly larger than the Ti^{4+} ion ($r = 0.75$ Å).[19,31] Figure 2d shows the UV/Vis diffuse reflectance spectra of TG and the Fe–TG samples. The onset of the absorption spectrum for TG appears at about 378 nm in the ultraviolet region, whereas, with increasing Fe^{3+} content in the Fe–TG sample, the onset of the absorption is gradually shifted to the visible region and a band between 400 and 500 nm shows up due to a d–d transition in Fe^{3+}. This result is in agreement with the colour change of the as-synthesised Fe–TG from pale-yellow to yellow with increasing doping content of Fe^{3+}. On the other hand, manganese-doping does not lead to an obvious change in the UV/Vis diffuse reflectance spectra of Mn–TG samples owing to a weak d–d transition in Mn^{2+}. To further reveal the effect of doping on the TG compound, ESR spectroscopy was employed to study the Fe–TG and Mn–TG samples. No signals from paramagnetic species were observed for the undoped TG. However, all samples after iron-doping (Fig-

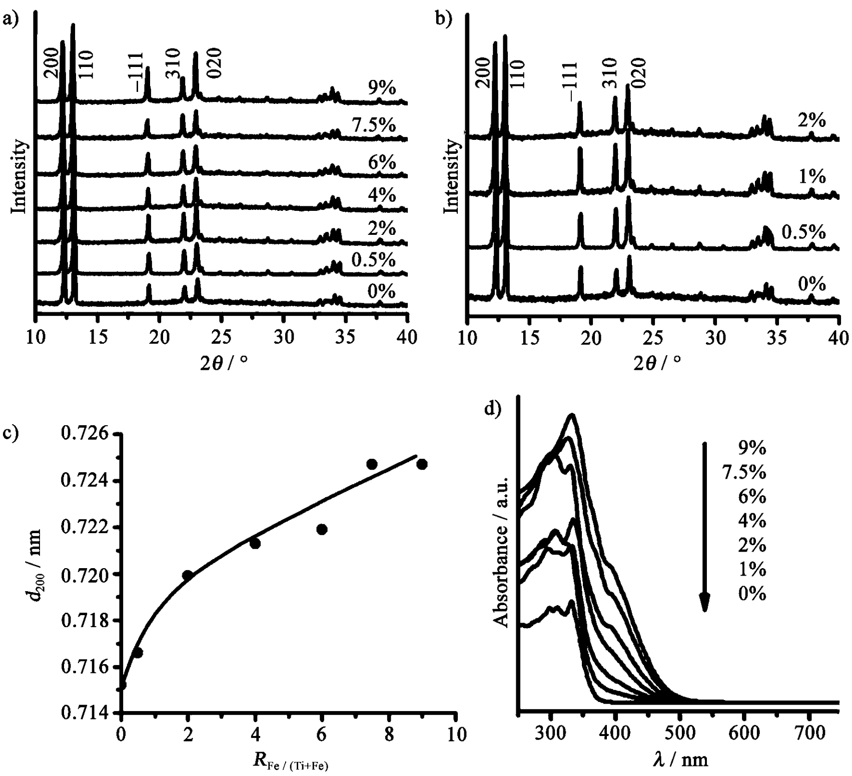

Figure 2. X-ray diffraction patterns of a) Fe–TG with different $R_{Fe/(Ti+Fe)}$ and b) Mn–TG with different $R_{Mn/(Ti+Mn)}$, c) value of d_{200} as a function of $R_{Fe/(Ti+Fe)}$ and d) the UV/Vis diffuse reflectance spectra of Fe–TG with different R_{Fe}/(Ti+Fe).

ure 3a) show a signal at $g = 4.27$, which is attributed to Fe^{3+} substituted for Ti^{4+} in the TG lattice. A similar signal has previously been observed in iron-doped TiO_2 and was assigned to Fe^{3+} in the Ti^{4+} position of the TiO_2 lattice.[32,33] A six-line spectrum characteristic of isolated paramagnetic Mn^{2+} (Figure 3b), which arises from the hyperfine interaction with the ^{55}Mn nuclear spin ($I = 5/2$), was observed for all samples after manganese-doping.[31,34]

Figure 4 shows the SEM and TEM images of the Fe–TG and Mn–TG samples, which exhibit rod shapes with diameters ranging from 250 nm to 1 μm and a length ranging from 1 to 10 μm. The rod surface appears to be smooth for both the Fe–TG and Mn–TG samples.

Inhibition effect of Fe^{3+} and Mn^{2+} on the crystallisation of M–TG: The effect of Fe^{3+} on the crystallisation of Fe–TG is so distinct that the crystallisation time can be estimated by observing the appearance of the solid product. The crystallisation time measured as a function of $R_{Fe/(Ti+Fe)}$ is presented in Figure 5. It can be seen that the crystallisation time of Fe–TG is prolonged from 4 min for undoped TG to 60 min for 9% Fe–TG. This inhibition effect of Fe^{3+} on the TG crystal-

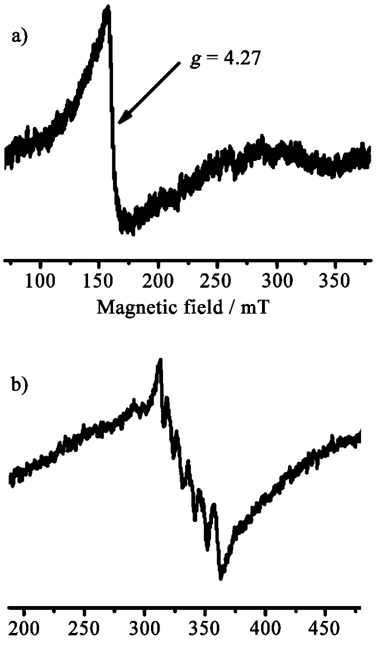

Figure 3. The electron spin resonance (ESR) spectra of a) 1% Fe–TG and b) 1% Mn–TG measured at room temperature.

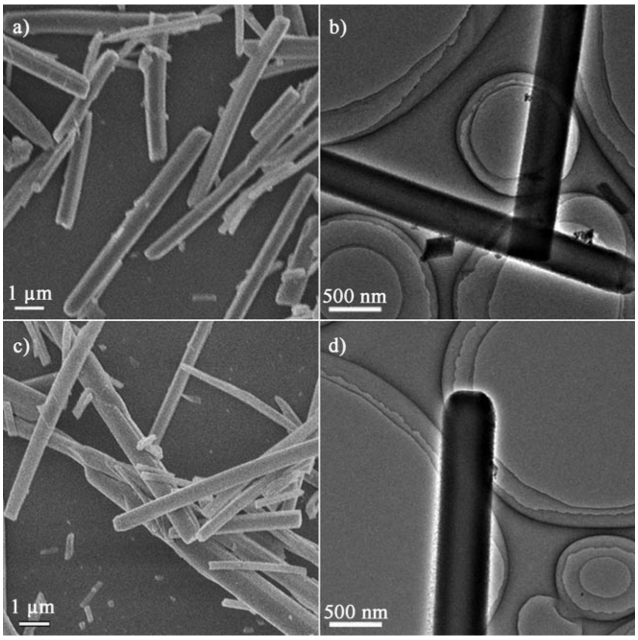

Figure 4. a) SEM and b) TEM images of the 0.5% Fe–TG sample and c) SEM and d) TEM images of the 0.5% Mn–TG sample.

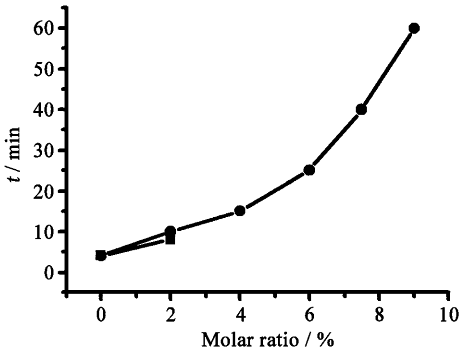

Figure 5. Crystallisation time as a function of $R_{\mathrm{Fe/(Ti+Fe)}}$ (●) and $R_{\mathrm{Mn/(Ti+Mn)}}$ (■).

lisation is correlated with a phase transition from solvated precursor ions or molecules to the solid-state crystalline product in accord with a classical nucleation model.[31,35] In this model, the driving force for spontaneous phase transition is parametrised by ΔFv, the difference in free energy between the solvated and crystalline forms of the material. For the precipitation of large crystals from solution, ΔFv dominates the overall change in free energy. The overall free energy change for crystallisation, which is proportional to the crystal volume V, is thus described by the equation $\Delta G = V\Delta Fv$. As shown in Figure 2, the substitution of Fe^{3+} for Ti^{4+} leads to a shift of the XRD peaks, which shows the introduction of strain into the crystal lattice caused by the substitution. Dopant-induced lattice strain reduces the thermodynamic driving force by reducing ΔFv, which directly results in a decrease of the crystallisation rate. Therefore, the time for Fe–TG to achieve full crystallisation is distinctly longer than that for TG, especially for a Fe–TG compound with a high $R_{\mathrm{Fe/(Ti+Fe)}}$ ratio.

Mn^{2+} shows a similar but smaller inhibition effect on the crystallisation of TG (Figure 5). In addition, the maximum amount of Mn^{2+} incorporated into the TG lattice seems to be much less than that of Fe^{3+}. No matter how much Mn^{2+} is added to the reaction mixture, the $R_{\mathrm{Mn/(Ti+Mn)}}$ value measured for the final Mn–TG product does not exceed 2%, and the crystallisation time of the Mn–TG remains about 10 min.

Preparation of porous M–TiO_2 using M–TG as precursors: M–TiO_2 (M = Fe, Mn) was formed by calcining M–TG at elevated temperatures. The XRD patterns of the samples obtained by calcining 0.5% Fe–TG at different temperatures are shown in Figure 6a. No impurity phases were detected apart from the anatase and rutile TiO_2. With an increase in calcination temperature, the Fe–TG precursor is first converted into an amorphous phase, which is subsequently transformed into anatase and then to rutile. At 300 °C, the calcined product is dominated by the amorphous phase, whereas at 450 °C the material (Fe–TiO_2) is identified as pure anatase. After calcination at 550 °C, the Fe–TiO_2 product contains both anatase (65%) and rutile (35%). A calcination temperature of 650 °C or above leads to the formation of the pure rutile phase. The XRD patterns for the Fe–TiO_2 samples with different $R_{\mathrm{Fe/(Ti+Fe)}}$ values obtained at 400 °C are shown in Figure 6b. The crystal size of the samples was estimated by using the Scherrer formula to be around 6 nm. The calcined product was identified as pure anatase even with an iron-doping content of 9%. It is known that anatase is mesostable compared with rutile[1] and Fe^{3+}-doping usually results in the transformation of anatase to rutile owing to the introduction of defects by doping.[15,36–39] However, in our experiment, the anatase phase was completely maintained after the thermal conversion of Fe–TG into Fe–TiO_2. Similarly, pure anatase Mn–TiO_2 (Figure S2 in the Supporting Information) can also be obtained by calcining Mn–TG at 400 °C.

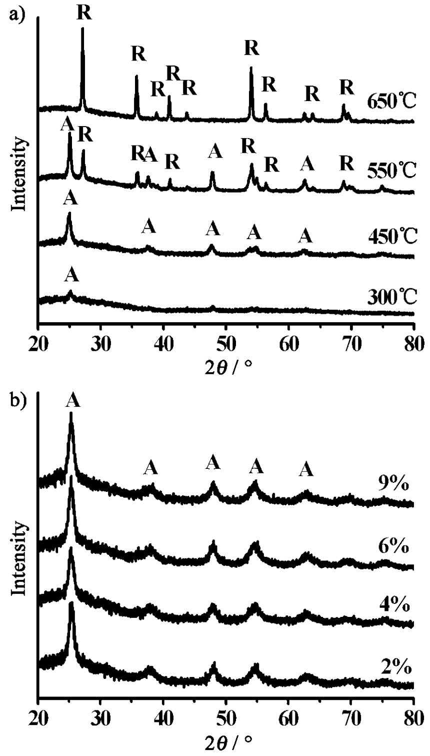

Figure 6. XRD patterns for a) 0.5% Fe–TiO_2 obtained at different temperatures and b) Fe–TiO_2 with different $R_{\mathrm{Fe/(Ti+Fe)}}$ obtained at 400 °C. A and R denote anatase and rutile, respectively.

The ESR spectra (Figure 7), which give valuable information about lattice sites at which paramagnetic dopant ions are located, of several calcined samples were recorded at room temperature. The two signals (Figure 7a) observed for 0.5% Fe–TiO_2 obtained at 400 °C are attributed to Fe^{3+} substituted for Ti^{4+} in the TiO_2 anatase lattice ($g = 1.99$) and to Fe^{3+} at the Ti^{4+} position adjacent to a charge-compensating oxygen vacancy ($g = 4.27$).[16,33] At a calcination temperature of 500 °C, four new peaks (Figure 7b) appear besides the two at $g = 1.99$ and 4.27. The new peaks at $g = 8.18$, 5.64, 3.43 and 2.60 have been assigned to Fe^{3+} ions substituted for Ti^{4+} in the TiO_2 rutile lattice.[40]

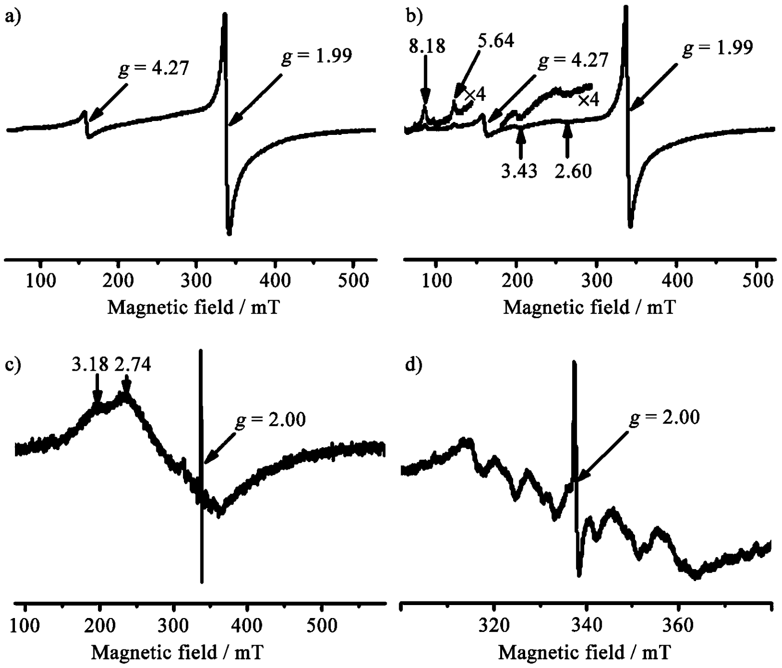

Figure 7. ESR spectra measured at room temperature for a) 0.5% Fe–TiO_2 obtained at 400°C, b) 0.5% Fe–TiO_2 obtained at 500°C, c) 0.5% Mn–TiO_2 obtained at 400°C and d) the signal at $g=2.00$ superimposed on the six-line splitting signal of Mn^{2+}.

Compared with that of the corresponding Mn–TG sample, the ESR spectrum of 0.5% Mn–TiO_2 obtained at 400°C (Figure 7c) is composed of three components. First, six hyperfine splitting lines (Figure 7d) attributed to Mn^{2+} substituted for Ti^{4+} in TiO_2 are observed. Secondly, there appear two peaks at $g=3.18$ and 2.74, which are assignable to Mn^{3+}. It is presumed that a small proportion of Mn^{2+}, especially on and near the surface of the microcrystals, have been oxidised to Mn^{3+} during calcination in air, meanwhile the rest of the Mn^{2+} ions remain in the bulk of the crystals. Finally, a new and sharp signal at $g=2.00$ appears to be superimposed on the six-line splitting signal of Mn^{2+}. A similar signal has also been observed previously in a Mn^{2+}-doped ZnO thin film and was attributed to the existence of p-type defects.[41] For Mn–TiO_2, the substitutional doping of Mn^{2+} ions into TiO_2 can easily generate p-type defects due to the lower oxidation state of Mn^{2+} compared with Ti^{4+}. When the Mn–TiO_2 sample is further calcined at 550°C for another 2 h, the signal at $g=2.00$ completely disappears, whereas other signals associated with Mn^{2+} and Mn^{3+} still remain. This is because the p-type defects can react with O_2 during calcination in air. Therefore, the signal at $g=2.00$ in Mn–TiO_2 can also be attributed to the presence of p-type defects.

The N_2 adsorption/desorption isotherms (Figure 8a) for the 0.25% Fe–TiO_2 samples obtained through calcination at 400 and 500°C are characteristic type-IV curves with H1-type hysteresis loops, indicative of the mesoporous structure of the materials. The Barrett–Joyner–Harlenda (BJH) pore size distributions (Figure 8a, inset) calculated on the basis of the desorption branches of the isotherms show peaks centred at ≈7 and ≈11.5 nm for the samples calcined at 400 and 500°C, respectively. The corresponding BET surface areas are ≈92 and ≈41 m^2g^{-1}. It can be seen that the smaller pores disappear and the surface area of the material is reduced when the calcination temperature is increased from 400 to 500°C. The loss of surface area with increasing calcination temperature is depicted in Figure 8b. In addition, the surface area of 0.25% Fe–TiO_2 is close to that of 0.25% Mn–TiO_2 at a certain calcination temperature.

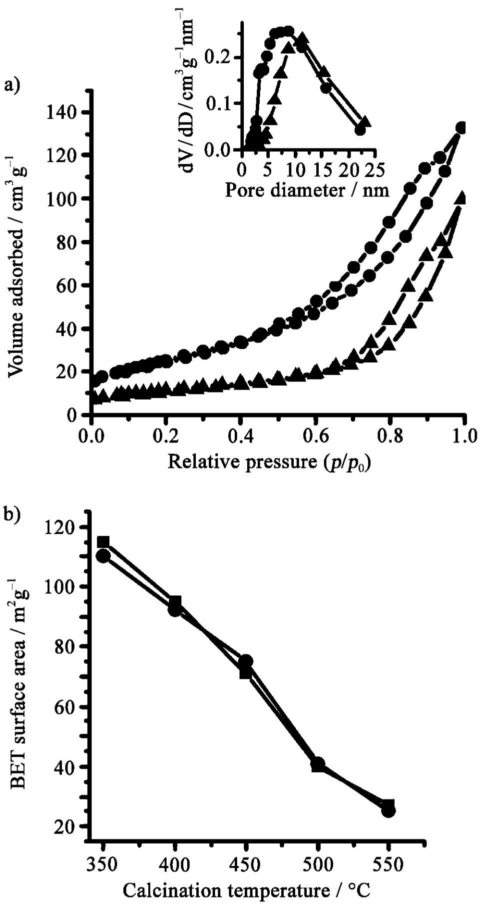

Figure 8. a) N_2 adsorption/desorption isotherms for 0.25% Fe–TiO_2 obtained at 400 and 500°C with the corresponding BJH pore size distributions shown in the inset and b) the effect of calcination temperature on surface area of 0.25% Fe–TiO_2 (●) and 0.25% Mn–TiO_2 (■).

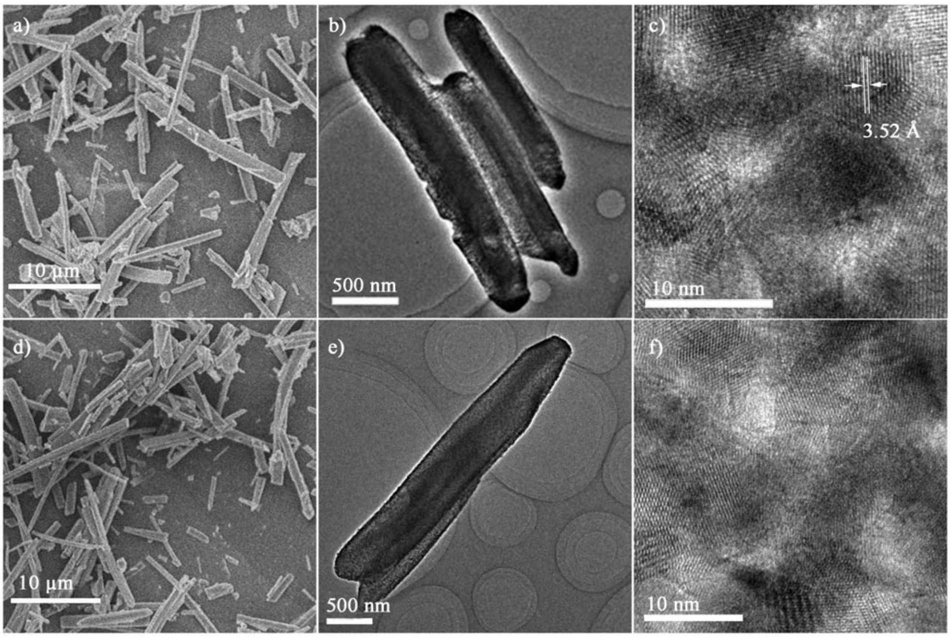

Figure 9. a) SEM, b) TEM and c) HRTEM images of 0.25% Fe–TiO_2 obtained at 400°C; d) SEM, e) TEM and f) HRTEM images of 0.25% Mn–TiO_2 obtained at 400°C.

To further verify the presence of porous structures in calcined Fe–TiO_2 and Mn–TiO_2, their SEM, TEM and HRTEM images were obtained. The SEM images (Figure 9a and d) reveal that the Fe–TiO_2 and Mn–TiO_2 materials obtained maintain the rod-like morphology of the precursors. The low-magnification TEM images of typical samples of 0.25% Fe–TiO_2 and 0.25% Mn–TiO_2 calcined at 400°C (Figure 9b and e) confirm that a porous feature is indeed present. The HRTEM images (Figure 9c and f) clearly show that nanocrystals are randomly arranged and interconnected to form irregular mesopores in the individual rod. The observed lattice spacing is about 3.52 Å, which corresponds to the distance between the (101) crystal planes of the anatase phase.

Photocatalytic performances of M–TiO_2 materials: The photocatalytic performances of the porous Fe–TiO_2 and Mn–TiO_2 materials were evaluated by testing the degradation of phenol under UV irradiation. The effect of calcination temperature on photocatalytic activity (Figure 10a) was elucidated by fixing the content of iron- or manganese-doping (0.25%). Evidently the variation in photocatalytic activity with increasing calcination temperature is similar for Fe–TiO_2 and Mn–TiO_2. The phenol conversion reaches a maximum of 100% for 0.25% Fe–TiO_2 or of 85% for 0.25% Mn–TiO_2 when the calcination temperature is 400°C. Further increases in the calcination temperature lead to a marked decrease in the phenol conversion from 100% at 400°C to 30% at 550°C for 0.25% Fe–TiO_2. This decrease in activity arises because the further increases in calcination temperature cause a significant decrease in the active surface area of the material (Figure 8a) and an increase in the amount of rutile, which has a lower photocatalytic activity than anatase (Figure 6a).[1] Compared with that obtained at 350°C, the sample obtained at 400°C has a higher photocatalytic activity although its surface area (92 $m^2 g^{-1}$) is smaller than that of the material treated at 350°C (110 $m^2 g^{-1}$). According to the XRD patterns (Figure 6b) and the HRTEM image (Figure 9c), the Fe–TiO_2 material obtained at 400°C is highly crystalline and its crystallinity is distinctly higher than that of the sample obtained at 350°C (Figure S3 in the Supporting Information). Thus, the enhanced photocatalytic activity for the sample obtained at 400°C is attributable to the higher crystallinity of the material.[42] The effect of iron-doping on photocatalytic activity (Figure 10b) was also elucidated by fixing the calcination temperature at 400°C. At this temperature the structure of the material is pore-rich and the crystallinity is high. The phenol conversion obtained with the undoped TiO_2 material under identical conditions is about 80%, whereas the conversion with 0.25% Fe–TiO_2 is 100%. Further increasing the amount of Fe^{3+} decreases the phenol conversion to a certain extent, but the minimum conversion is still higher than 80%. For Mn–TiO_2, the photocatalytic conversion of phenol reaches a maximum of 90% when $R_{Mn/(Ti+Mn)}$ is 0.5%. For both Fe–TiO_2 and Mn–TiO_2 there is an optimal dopant concentration above which the photocatalytic activity decreases again. Generally, the recombination rate depends on the distance separating the electron–hole pair.[19] The recombination rate increases with dopant concentration because the distance between trapping sites in a particle decreases with increasing dopant concentration.

The changes in phenol concentration over the course of the photodegradation reaction (Figure 10c) indicate that the porous 0.25% Fe–TiO_2 is photocatalytically more active than the commercial titania photocatalyst P25. The excellent stability of the 0.25% Fe–TiO_2 photocatalyst was demonstrated by a recycling experiment (Figure 10d). After five cycles of the photocatalytic degradation of phenol, there was no loss of photocatalytic activity. Figure 10e shows that the Fe–TiO_2 particles settle more quickly in an aqueous suspension than the P25 photocatalyst nanocrystals. This result, in combination with that of the recycling experiment, demonstrates that the TiO_2 photocatalysts synthesised through our approach can be easily separated and recovered after photocatalytic reactions.

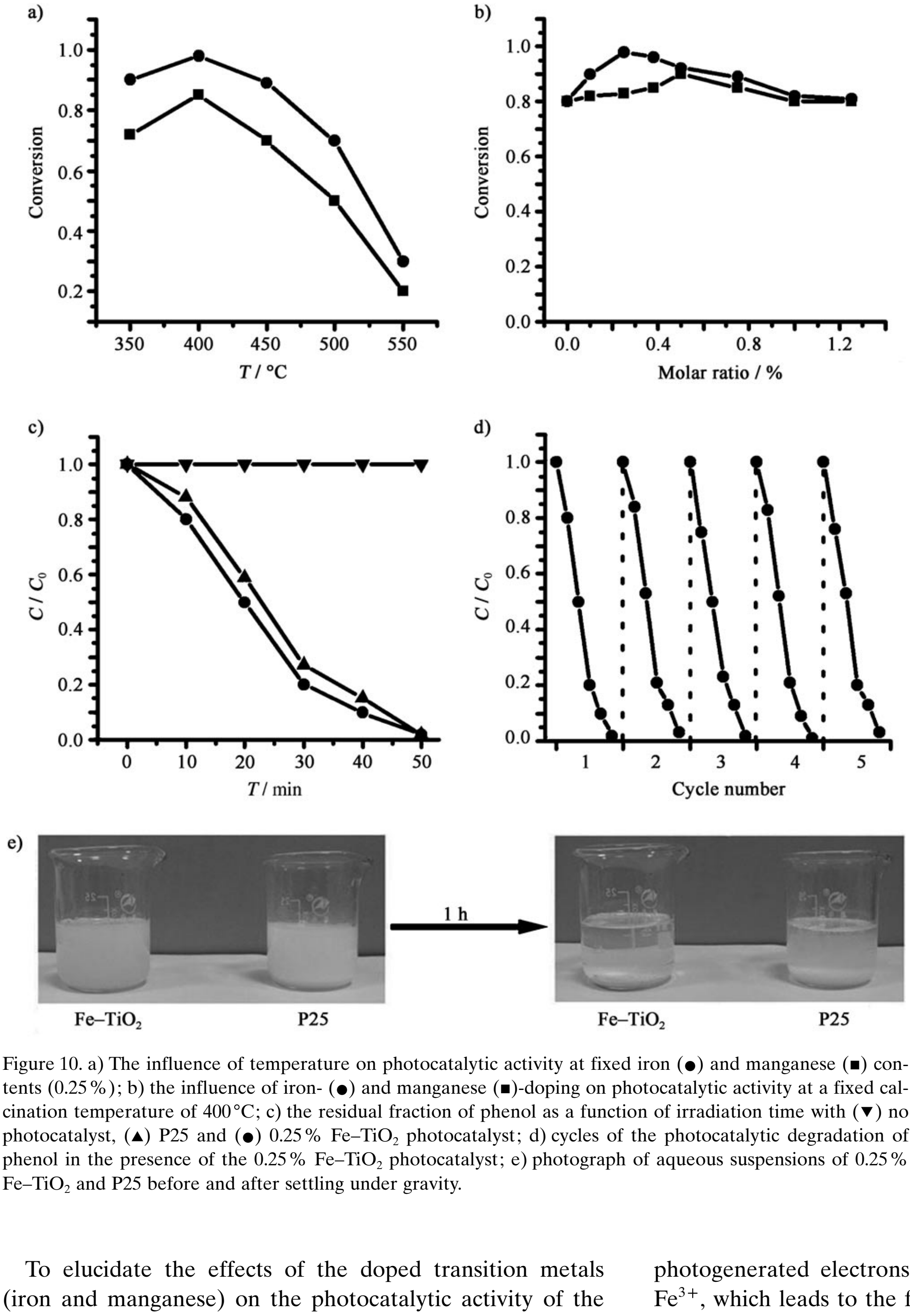

Figure 10. a) The influence of temperature on photocatalytic activity at fixed iron (●) and manganese (■) contents (0.25 %); b) the influence of iron- (●) and manganese (■)-doping on photocatalytic activity at a fixed calcination temperature of 400 °C; c) the residual fraction of phenol as a function of irradiation time with (▼) no photocatalyst, (▲) P25 and (●) 0.25 % Fe–TiO_2 photocatalyst; d) cycles of the photocatalytic degradation of phenol in the presence of the 0.25 % Fe–TiO_2 photocatalyst; e) photograph of aqueous suspensions of 0.25 % Fe–TiO_2 and P25 before and after settling under gravity.

To elucidate the effects of the doped transition metals (iron and manganese) on the photocatalytic activity of the resultant TiO_2 material, electron-transfer behaviour in M–TiO_2 under UV irradiation was investigated. The ESR spectra of 0.5 % Fe–TiO_2 obtained in the dark and under UV irradiation are displayed in Figure 11a–c and those of 0.5 % Mn–TiO_2 are shown in Figure 11d–f. For undoped TiO_2, there are no signals from paramagnetic species in either the dark or under UV irradiation. When the ESR spectrum of Fe–TiO_2 was recorded in the dark, two signals, attributed to Fe^{3+} substituted for Ti^{4+} in the anatase lattice ($g=1.99$) and to Fe^{3+} in the lattice adjacent to a charge-compensating oxygen vacancy ($g=4.27$), show up distinctly. After UV irradiation for 2 min, the intensities of the signals at both $g=4.27$ and 1.99 decrease simultaneously. As the irradiation time is prolonged to 4 min, the intensities of the Fe^{3+} signals do not decrease further. Similar results have been observed previously.[32,33] The simultaneous decrease of the two signals is due to the concurrent trapping of holes and electrons by the different Fe^{3+} sites. The hole is trapped at the Fe^{3+} site adjacent to a charge-compensating oxygen vacancy, whereas the electron is trapped at the other type of Fe^{3+} site.[33] In addition, it was noted that there are no Ti^{3+} signals observed during the irradiation process, which suggests that Fe^{3+} ions are better electron traps than Ti^{4+} ions. When the ESR spectrum of Mn–TiO_2 was measured under UV irradiation, the Mn^{2+} signals characteristic of six hyperfine splitting lines were weakened and the Mn^{3+} signals at $g=3.18$ and 2.74 were strengthened. This suggests that Mn^{2+} is oxidised to Mn^{3+} by trapping the photoexcited hole in the valence band of TiO_2.

Charge-trapping in the transition-metal ion centre is conducive to separation of the photogenerated electron–hole pairs, which leads to an enhancement of the photocatalytic activity for the metal-doped TiO_2. Under UV irradiation, electron–hole pairs are produced in the conduction and valence bands of TiO_2. For Fe–TiO_2, the photogenerated electrons can be transferred from TiO_2 to Fe^{3+}, which leads to the formation of Fe^{2+} [Eq. (1)]. Meanwhile, Fe^{3+} can also serve as a hole trap [Eq. (2)].

$$Fe^{3+} + e^{-} \rightarrow Fe^{2+} \tag{1}$$

$$Fe^{3+} + h^{+} \rightarrow Fe^{4+} \tag{2}$$

In contrast to Fe^{3+}, which can act as both electron and hole traps, Mn^{2+} can only act as a hole trap [Eq. (3)]. Generally, trapping a hole alone to separate photogenerated electron–hole pairs is of low efficiency because the trapped hole may quickly recombine with its mobile counterpart [photogenerated electron; Eq. (4)].[18,19] This explains why

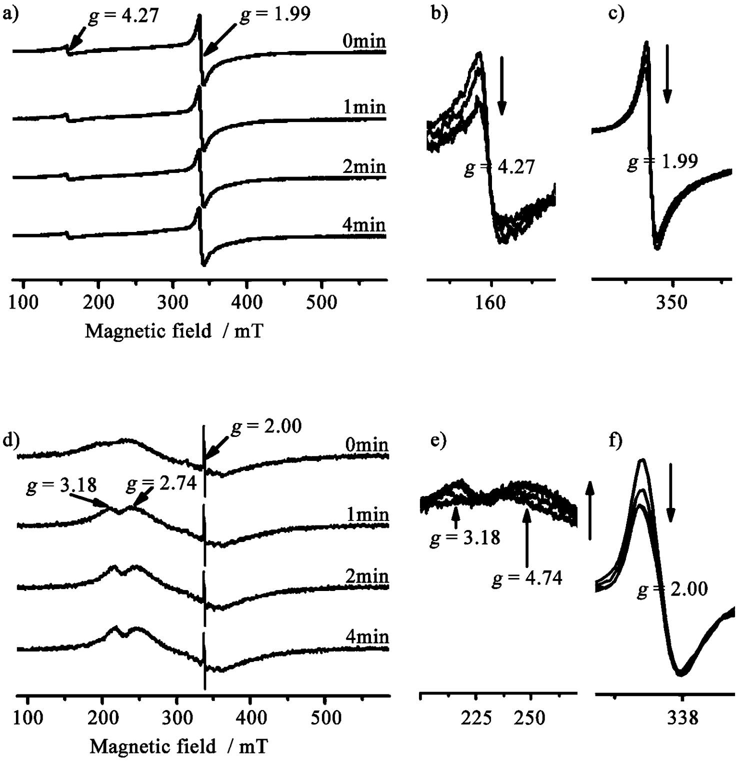

Figure 11. a) ESR spectra of 0.5% Fe–TiO_2 recorded at room temperature before and after UV irradiation for 1, 2 and 4 min; b) the change in intensity of the signal at $g=4.27$ with increasing irradiation time; c) the change in intensity of the signal at $g=1.99$ with increasing irradiation time; d) ESR spectra of 0.5% Mn–TiO_2 measured at room temperature before and after UV irradiation for 1, 2 and 4 min; e) the change in intensity of the signals at $g=3.18$ and 4.74 with increasing irradiation time; f) the change in intensity of the signal at $g=2.00$ with increasing irradiation time. (↓) denotes the decrease in signal intensity with increasing irradiation time and (↑) denotes the increase in signal intensity with increasing irradiation time.

Fe–TiO_2 shows higher photocatalytic activity than Mn–TiO_2.

$$Mn^{2+} + h^{+} \rightarrow Mn^{3+} \quad (3)$$

$$Mn^{3+} + e^{-} \rightarrow Mn^{2+} \quad (4)$$

Conclusion

Herein we have reported a doping strategy that realises the formation of non-stoichiometric titanium-based heterometal alkoxides (M–TG, with M = Fe, Mn) for the first time. Furthermore, by using these heterometal alkoxides as single-source precursors, crystalline porous M–TiO_2 photocatalysts have been directly obtained by a simple thermal treatment process. Investigations into the photocatalytic activities of the as-prepared M–TiO_2 materials reveal that high crystallinity, a large surface area and appropriate transition-metal-doping are all beneficial to the enhancement of the photocatalytic activity of the doped TiO_2 materials. Compared with Mn–TiO_2, Fe–TiO_2 shows greater photocatalytic activity due to a greater inhibition effect of Fe^{3+} on the recombination of photogenerated electron–hole pairs. It has been proven that the combination of porosity with metal-doping leads to highly effective TiO_2-based photocatalysts that are easy to separate from the corresponding reaction systems. The successful synthesis of non-stoichiometric heterometal alkoxides and their conversion into porous oxide materials opens the way not only to the synthesis of new metal alkoxides, but also to heterometal oxides with useful functions.

Experimental Section

Materials: Absolute ethanol, chromium(III) chloride hexahydrate, iron(III) chloride hexahydrate, manganese(II) chloride tetrahydrate, nickel(II) chloride hexahydrate, cobalt(II) chloride hexahydrate and copper(II) chloride dihydrate were all purchased from Beijing Chemical Factory. All the reagents were of analytical grade and used as received. Titanium(IV) *n*-butoxide was purchased from Tianjin Guangfu Fine Chemical Research Institute. Titania P25 with an average crystal size of 21 nm and a BET surface area of $(50 \pm 15)\,m^2g^{-1}$ was purchased from Beijing Entrepreneur Science & Trading Co., Ltd.

Synthesis of M–TG: In a typical synthesis titanium(IV) *n*-butoxide (1 mL, 3 mmol) as the titanium source and iron(III) chloride hexahydrate (x mmol, $0 \leq x \leq 0.3$ mmol) as the iron source were added to ethylene glycol (10 mL) and heated at 180 °C for 2–5 h under vigorous stirring to form Fe–TG. The reaction time was prolonged with increasing $R_{Fe/(Ti+Fe)}$. After cooling to room temperature, the yellow Fe–TG precipitate was washed several times with ethanol and dried naturally at room temperature. By using a similar procedure, Mn^{2+} was also incorporated into the TG structure to form Mn–TG. For comparison, attempts were made to replace Fe^{3+} as dopant by a series of 3d transition metals, including Cr^{3+}, Co^{2+}, Ni^{2+} and Cu^{2+}, under identical reaction conditions. The ratio between the 3d transition metal and the total metal content was 0.5%. No M–TG products were obtained in these cases.

Composition analysis: For composition analysis, the as-prepared powder samples were repeatedly washed with absolute ethanol and dissolved in dilute hydrochloric acid. The results of the quantitative elemental analysis indicated that the Fe/(Ti+Fe) and Mn/(Ti+Mn) atomic ratios in the as-prepared materials were very close to the nominal values of the metal sources used. Thus, the Fe/(Ti+Fe) and Mn/(Ti+Mn) atomic ratios in the obtained powder samples were quoted as those of the metal sources used. In addition, the Cr/(Ti+Cr), Co/(Ti+Co), Ni/(Ti+Ni) and Cu/(Ti+Cu) atomic ratios were 0.009, 0.012, 0.005 and 0.013%, respectively. Therefore, it was presumed that the TG compound was not doped with Cr^{3+}, Co^{2+}, Ni^{2+} and Cu^{2+}.

Synthesis of porous M–TiO_2: M–TiO_2 was obtained by calcining the M–TG precursor in a muffle furnace at the appropriate temperature for 2 h.

Photocatalytic activity: The photocatalytic activity was investigated in aqueous solution in a water-cooled quartz cylindrical cell with a 1 cm optical path length. The reaction mixture in the cell was maintained at ≈20 °C by a continuous flow of water and magnetic stirring, and was illuminated with an internal light source. The UV source was a 400 W high-pressure mercury lamp (main output 313 nm).

The Fe–TiO_2 photocatalyst (0.8 g) was mixed with an aqueous solution of phenol (700 mL, 4.0×10^{-4} M). The aqueous system was magnetically stirred in the dark for 30 min to allow an adsorption equilibrium between the phenol and the catalyst to be formed and then subjected to UV irradiation. Each reaction cycle lasted 50 min during which oxygen was bubbled through the solution. At given irradiation time intervals, a series of aqueous solutions (3 mL) were collected and filtered through a Millipore filter to remove the suspended catalyst particles for analysis. The concentration of the phenol was analysed on a UV/Vis spectrophotometer using its characteristic absorption at 270 nm. For comparison, the photocatalytic activity of commercial photocatalyst P25 was also measured under the same conditions. The weights of all the catalyst samples were exactly the same.

General characterisation: The powder XRD patterns were recorded on a Rigaku D/Max 2550 X-ray diffractometer with $Cu_{K\alpha}$ radiation (λ = 1.5418 Å). The scanning SEM images were recorded on a JEOL JSM 6700F electron microscope, whereas the TEM and high-resolution TEM (HRTEM) images were obtained on a JEOL JSM-3010 TEM microscope. The concentration of phenol was analysed with a Shimadzu UV-2450 spectrophotometer, whereas the UV/Vis diffuse reflectance spectra were recorded on a Perkin–Elmer Lambda 20 UV/Vis spectrometer. The absorbance spectra were obtained from the reflectance spectra by Kubelka–Munk transformations. The nitrogen adsorption and desorption isotherms were measured by using a Micromeritics ASAP 2020M system, whereas the ESR spectra were obtained on a JES-FA 200 ESR spectrometer. A 500 W high-pressure mercury lamp was used as an irradiation light source for in situ ESR measurements. The elemental analyses were performed on a Perkin-Elmer Optima 3300DV ICP instrument.

Acknowledgements

This work was financially supported by the National Basic Research Program (2007CB613303) and the NSFC (20731003).

---

[1] X. B. Chen, S. S. Mao, *Chem. Rev.* **2007**, *107*, 2891–2959.
[2] A. L. Linsebigler, G. Lu, J. T. Yates, Jr., *Chem. Rev.* **1995**, *95*, 735–758.
[3] A. Rachel, M. Subrahmanyam, P. Boule, *Appl. Catal. B Environ.* **2002**, *37*, 301–308.
[4] J. A. Byrne, B. R. Eggins, N. M. D. Brown, B. McKinncy, M. Rouse, *Appl. Catal. B* **1998**, *17*, 25–36.
[5] Z. Y. Liu, D. D. Sun, P. Guo, J. O. Leckie, *Chem. Eur. J.* **2007**, *13*, 1851–1855.
[6] X. Z. Li, H. Liu, L. F. Cheng, H. T Tong, *Environ. Sci. Technol.* **2003**, *37*, 3989–3994.
[7] B. L. Zhang, B. S. Chen, K. Y. Shi, S. J. He, X. D. Liu, Z. J. Du, K. L. Yang, *Appl. Catal. B* **2003**, *40*, 253–258.
[8] D. G. Shchukin, R. A. Caruso, *Chem. Mater.* **2004**, *16*, 2287–2292.
[9] G. J. A. A. Soler-Illia, C. Sanchez, B. Lebean, J. Patarin, *Chem. Rev.* **2002**, *102*, 4093–4138.
[10] S. Y. Choi, M. Mamak, N. Coombs, N. Chopra, G. A. Ozin, *Adv. Funct. Mater.* **2004**, *14*, 335–344.
[11] W. Y. Dong, Y. J. Sun, C. W. Lee, W. M. Hua, X. C. Lu, Y. F. Shi, S. C. Zhang, J. M. Chen, D. Y. Zhao, *J. Am. Chem. Soc.* **2007**, *129*, 13894–13904.
[12] D. L. Li, H. S. Zhou, I. Honma, *Nat. Mater.* **2004**, *3*, 65–72.
[13] W. Y. Teoh, R. Amal, L. Mädler, S. E. Pratsinis, *Catal. Today* **2007**, *120*, 203–213.
[14] M. I. Litter, J. A. Navío, *J. Photochem. Photobiol. A* **1996**, *98*, 171–181.
[15] F. Gracia, J. P. Holgado, A. Caballero, A. R. Gonzalez-Elipe, *J. Phys. Chem. B* **2004**, *108*, 17466–17476.
[16] K. Nagaveni, M. S. Hegde, G. Madras, *J. Phys. Chem. B* **2004**, *108*, 20204–20212.
[17] J. Zhu, J. Ren, Y. N. Huo, Z. F. Bian, H. X. Li, *J. Phys. Chem. C* **2007**, *111*, 18965–18969.
[18] J. Zhu, W. Zheng, B. He, J. Zhang, M. Anpo, *J. Mol. Cat. A* **2004**, *216*, 35–43.
[19] W. Choi, A. Termin, M. R. Hoffman, *J. Phys. Chem.* **1994**, *98*, 13669–13679.
[20] X. Fan, X. Chen, S. Zhu, Z. Li, T. Yu, J. Ye, Z. Zou, *J. Mol. Catal. A* **2008**, *284*, 155–160.
[21] D. C. Brudley, *Chem. Rev.* **1989**, *89*, 1317–1322.
[22] C. D. Chandler, C. Roger, M. J. Hampden-Smith, *Chem. Rev.* **1993**, *93*, 1205–1241.
[23] C. Sanchez, B. Julián, P. Belleville, M. Popall, *J. Mater. Chem.* **2005**, *15*, 3559–3592.
[24] D. Larcher, G. Sudant, R. Patrice, J. M. Tarascon, *Chem. Mater.* **2003**, *15*, 3543–3551.
[25] K. G. Caulton, *Chem. Rev.* **1990**, *90*, 969–995.
[26] A. Singh, R. C. Mehrotra, *Coord. Chem. Rev.* **2004**, *248*, 101–118.
[27] L. G. Hubert-Pfalzgraf, *Coord. Chem. Rev.* **1998**, *178*, 967–997.
[28] D. Wang, R. Yu, N. Kumada, N. Kinomura, *Chem. Mater.* **1999**, *11*, 2008–2012.
[29] H. Deng, X. L. Li, Q. Peng, X. Wang, J. P. Chen, Y. D. Li, *Angew. Chem.* **2005**, *117*, 2842–2845; *Angew. Chem. Int. Ed.* **2005**, *44*, 2782–2785.
[30] X. H. Li, D. H. Zhang, J. S. Chen, *J. Am. Chem. Soc.* **2006**, *128*, 8382–8383.
[31] J. D. Bryan, D. R. Gamelin, *Prog. Inorg. Chem.* **2005**, *54*, 47–126.
[32] H. Ozaki, S. Iwamoto, M. Inoue, *J. Phys. Chem. C* **2007**, *111*, 17061–17066.
[33] M. Grätzel, R. F. Howe, *J. Phys. Chem.* **1990**, *94*, 2566–2572.
[34] Y. Yang, O. Chen, A. Angerhofer, Y. C. Cao, *J. Am. Chem. Soc.* **2006**, *128*, 12428–12429.
[35] D. W. Oxtoby, *Acc. Chem. Res.* **1998**, *31*, 91–97.
[36] Y. H. Zhang, A. Reller, *J. Mater. Chem.* **2001**, *11*, 2537–2541.
[37] N. Perkas, O. Palchik, I. Brukental, I. Nowik, Y. Gofer, Y. Koltypin, A. Gedanken, *J. Phys. Chem. B* **2003**, *107*, 8772–8778.
[38] J. A. Wang, R. Limas-Ballesteros, T. Lōpez, A. Moreno, R. Gōmez, O. Novaro, X. Bokhimi, *J. Phys. Chem. B* **2001**, *105*, 9692–9698.
[39] X. H. Wang, J. G. Li, H. Kamiyama, M. Katada, N. Ohashi, Y. Moriyoshi, T. Ishigaki, *J. Am. Chem. Soc.* **2005**, *127*, 10982–10990.
[40] J. Soria, J. C. Conesa, V. Augugliaro, L. Palmisano, M. Schiavello, A. Sclafani, *J. Phys. Chem.* **1991**, *95*, 274–282.
[41] N. S. Norberg, K. R. Kittilstved, J. E. Amonette, R. K. Kukkadapu, D. A. Schwartz, D. R. Gamelin, *J. Am. Chem. Soc.* **2004**, *126*, 9387–9398.
[42] V. F. Stone, Jr., R. J. Davis, *Chem. Mater.* **1998**, *10*, 1468–1474.

Received: June 23, 2008